physica status solidi a
www.pss-a.com

Achieving High Dielectric Constants in Tetragonal Single-Phase $ZrHfO_2$ Thin Films through the Atomic Layer Deposition Process Using a Mixed Precursor

Jenam Kim, Young Uk Ryu, Ae Jin Lee, Ye Won Kim, Ji Hyeon Hwang, Youngjin Kim, Hansol Oh, YongJoo Park, and Woojin Jeon**

Herein, the deposition of homogeneous $Zr_xHf_{(1-x)}O_2$ ($x < 1$) thin films for dynamic random-access memory (DRAM) capacitor dielectric layers by atomic layer deposition (ALD) using a mixed precursor mixture of two precursors is investigated. ZrO_2- and HfO_2-based thin films are widely used as capacitor dielectric layers because of their high dielectric constant (*k*) values and low leakage current properties. Herein, particularly, films with mixed structures of ZrO_2/HfO_2 are investigated because ZrO_2 supports the growth of HfO_2 in the tetragonal phase. However, the mixed structures deposited by ALD remain inhomogeneous even after the annealing process. The inhomogeneity results in part of the HfO_2 remaining in the monoclinic phase, which reduces the *k* value. Herein, the formation of homogeneous tetragonal-phase $Zr_xHf_{1-x}O_2$ using a mixed precursor consisting of CpZr and CpHf precursors is investigated. The formation of the tetragonal phase in the $Zr_xHf_{(1-x)}O_2$ thin films is determined through chemical and structural analysis. The variation of the electrical properties with the Zr/Hf concentration ratio is investigated. The electrical properties are enhanced compared to laminated ZrO_2/HfO_2 and single thin films.

1. Introduction

Dynamic random access memory (DRAM) has been an important memory device in the semiconductor industry over the past decades. As technology develops, the cell size needs to be further scaled down to achieve higher performance and lower power consumption. Numerous studies have therefore been performed on higher dielectric constant (*k*) materials for DRAM capacitor dielectric layers.[1–4] Among them, ZrO_2-based thin films, especially $ZrO_2/Al_2O_3/ZrO_2$ (ZAZ), have been used in recent DRAM technology because of their suitable *k* value, low leakage current, and compatibility with TiN.[5–10] However, although the leakage current is well controlled in ZAZ thin films, the *k* value in these films is decreased compared to other materials because of the low *k* value of Al_2O_3 ($k \approx 9$).[11] Therefore, alternative dielectric materials and structures to replace ZAZ have been investigated.

Rutile TiO_2 ($k \approx 100$) and $SrTiO_3$ ($k \approx 150$) have been extensively studied as high-*k* dielectric materials.[12–20] However, numerous issues need to be overcome. These materials have a small bandgap (E_g of approximately 3.0–3.2 eV), which results in high leakage current and necessitates the development of new electrode materials to replace TiN, which is mainly used as the electrode material.[21–23] HfO_2 has also been extensively studied as a representative high-*k* material for gate dielectric and DRAM capacitor dielectric applications.[24–26] Many studies have been performed to increase the *k* value of HfO_2,[27–34] for example, through the use of dopants such as carbon,[27] Si,[29] and Al_2O_3.[30,31,35] HfO_2 can exist in various crystal structures with different values of *k* such as the monoclinic ($k \approx 20$), orthorhombic ($k \approx 30$), cubic, and tetragonal structures ($k > 40$). In particular, the dielectric constant of tetragonal phase (*t*-phase) HfO_2 calculated by first-principles calculations in a previous work was approximately 70.[36,37] In general, a monoclinic structure has higher surface energy and lower bulk energy compared to cubic and tetragonal structures. For this reason, the tetragonal structure of HfO_2 is stable at the small grain size of approximately 3 nm, which is called the critical grain size.[28] However, the methods employed in the aforementioned studies could not completely transform the monoclinic phase (*m*-phase) into the t-phase. Meanwhile, ZrO_2 is more stable in the tetragonal phase than HfO_2, and has a critical grain size of 20 nm and similar chemical structure and properties to HfO_2.[28] It has been reported that alloying ZrO_2 with HfO_2 can stabilize the tetragonal structure because the grain size and lattice distortion of HfO_2 can be controlled by stable t-phase ZrO_2 through the template effect.[38] There have therefore been numerous studies on $Hf_xZr_{(1-x)}O_2$ mixed

J. Kim, Y. U. Ryu, A. J. Lee, Y. W. Kim, J. H. Hwang, Y. Kim, W. Jeon
Department of Advanced Materials Engineering for Information and Electronics, and Integrated Education Program for Frontier Science & Technology (BK21 Four)
Kyung Hee University
Yongin, Gyeonggi 17104, Korea
E-mail: woojin.jeon@khu.ac.kr

H. Oh, Y. J. Park
Advanced Research Development Team
SK Trichem Co. Ltd.
Sejong 30068, Korea
E-mail: yj.park81@sk.com

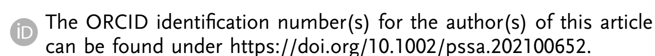
The ORCID identification number(s) for the author(s) of this article can be found under https://doi.org/10.1002/pssa.202100652.

DOI: 10.1002/pssa.202100652

 © 2022 Wiley-VCH GmbH

structures and HfO_2/ZrO_2 laminated structures for dielectric applications.[39–41]

Meanwhile, the employed thin-film deposition method also affected the crystal structure. In this regard, chemical vapor deposition would be favorable due to its relatively high process temperature, which could contribute to enhancing crystallinity. However, for the DRAM application, atomic layer deposition (ALD) is only the appropriate deposition technique for the high-k thin-film deposition due to the high aspect ratio of the DRAM capacitor structure. The fact that the ALD uses the chemisorption of precursor limits a process temperature below the temperature of thermal decomposition of precursor, resulting in relatively poor crystallinity of deposited thin film. Moreover, the ALD process is not adequate to deposit a multicomponent thin film. In general, each cycle in the ALD process consists of a precursor feeding-precursor purge-reactant feeding-reactant purge steps. The cycle is repeated to perform layer-by-layer deposition. To achieve doped or mixed structures in the ALD, supercycles consisting of dopant subcycles between the regular cycles are utilized.[42] The thin film deposited through this method has a laminated structure due to the characteristics of the layer-by-layer ALD deposition. Diffusion and crystallization are carried out by performing a postdeposition annealing (PDA) process to achieve the final doped or mixed structure. However, the dopant or mixture profile obtained through this process inevitably has local concentration gradients along the depth direction, which results in an inhomogeneous thin film.[43] This causes some issues where parts of the thin film may be partially undoped. Based on these considerations, the deposition of a homogeneous $Zr_xHf_{(1-x)}O_2$ thin film by ALD through the use of a mixture of the Zr precursor and the Hf precursor, which is so called a "mixed" precursor, is investigated in this work. In contrast to general ALD, the same concentration can be achieved at all positions because the precursors that are fed during the deposition process are already premixed. We systematically confirmed the homogeneity of the ALD thin films and examined the structural and chemical properties of various Zr compositions. We also confirmed the enhancement of their electrical properties through a comparison with other thin films.

2. Results and Discussion

The ALD process conditions of a mixed precursor consisting of cyclopentadienyl tris (dimethylamino) zirconium ($ZrCp[NMe_2]_3$, CpZr) as the Zr precursor and cyclopentadienyl tris (dimethylamino) hafnium ($HfCp[NMe_2]_3$, CpHf) as the Hf precursor were first investigated. The decomposition temperatures of CpZr and CpHf were measured by differential scanning calorimetry (DSC) to be 301 and 341 °C, respectively (data not shown). To determine the appropriate ALD deposition temperature of the mixed precursor, the growth per cycle (GPC) of the film as a function of the deposition temperature (220–380 °C) was investigated under the fixed process condition of 12–20–10–15 s precursor feeding-Ar purge-O_3 feeding-Ar purge cycles, at which each step was given more time than in the ALD process conditions mentioned earlier. At temperatures lower than 290 °C, the growth rate decreased to less than 0.126 nm cycle^{-1}, compared to the growth rate of 0.14–0.15 nm cycle^{-1} at 290–320 °C, which is the temperature window for self-limited ALD growth (**Figure 1**). In comparison, at temperatures higher than 320 °C, the growth rate increased to more than 0.18 nm cycle^{-1} because of the thermal decomposition of the precursors. Thus, the temperature range of 290–320 °C is appropriate for the ALD process, which is corroborated with the temperature window of the ALD process using CpZr and CpHf.[44,45] We fixed the temperature to 300 °C to achieve a high growth rate. To determine the ALD saturation condition at 300 °C, the various steps in the ALD cycle were given sufficient time for completion and determined in sequence starting from the precursor feeding time. Accordingly, the ALD saturation condition was determined to be 7–15–5–10 s (**Figure 2**a). The time was reduced from the 15–25–10–15 s and 10–10–7–15 s required for HfO_2 and ZrO_2 (Figure S1, Supporting Information), respectively. In addition, the superior accuracy of the GPC compared to those of ZrO_2 and HfO_2 was confirmed by measuring the thickness as a function of the number of cycles. Except for the initial growth, which was affected by the surface reactivity, the GPC of the deposited $ZrHfO_2$ was 0.136 nm cycle^{-1}, which was higher than those of ZrO_2 and HfO_2 (0.103 and 0.116 nm cycle^{-1}, respectively) (Figure 2b).

The compositions of the thin film synthesized with several precursor compositions were analyzed through X-ray photoelectron spectroscopy (XPS) analysis (**Figure 3** and S2a, Supporting Information). The relative Zr composition to the total metal-ion content of the deposited $ZrHfO_2$ (ZHO) thin film [Zr/(Zr + Hf)] was calculated using the concentration measured from the XPS depth profile at the etching time of 5 s (Figure 3a). As shown in Figure 3, Zr/(Zr + Hf) increased from 45.4 to 59.43, 63.87, 71.95, 75.08, and 77.67 at% at the mixed precursor Zr concentrations of 40, 50, 60, 65, 70, and 75 mol%, respectively. These were called 4-, 5-, 6-, 6.5-, 7-, and 7.5-ZHO, with the numbers indicating the relative Zr concentrations in the mixed precursor. Although there was a slight difference in the deposited concentration compared to the inlet concentration, the linear increase implies that the deposited concentration could be sufficiently controlled by adjusting the concentration of the mixed precursor via the liquid delivery system (see Experimental Section for the detail). The distribution of Zr and Hf cations in the thin film was confirmed using the energy-dispersive X-ray spectroscopy (EDX) of transmission electron microscopy (TEM) analysis (Figure 3b). As shown in EDX images for Zr and Hf, the deposited thin film

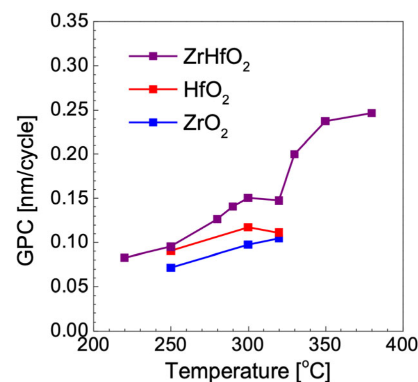

Figure 1. GPC values as a function of the process temperature.

© 2022 Wiley-VCH GmbH

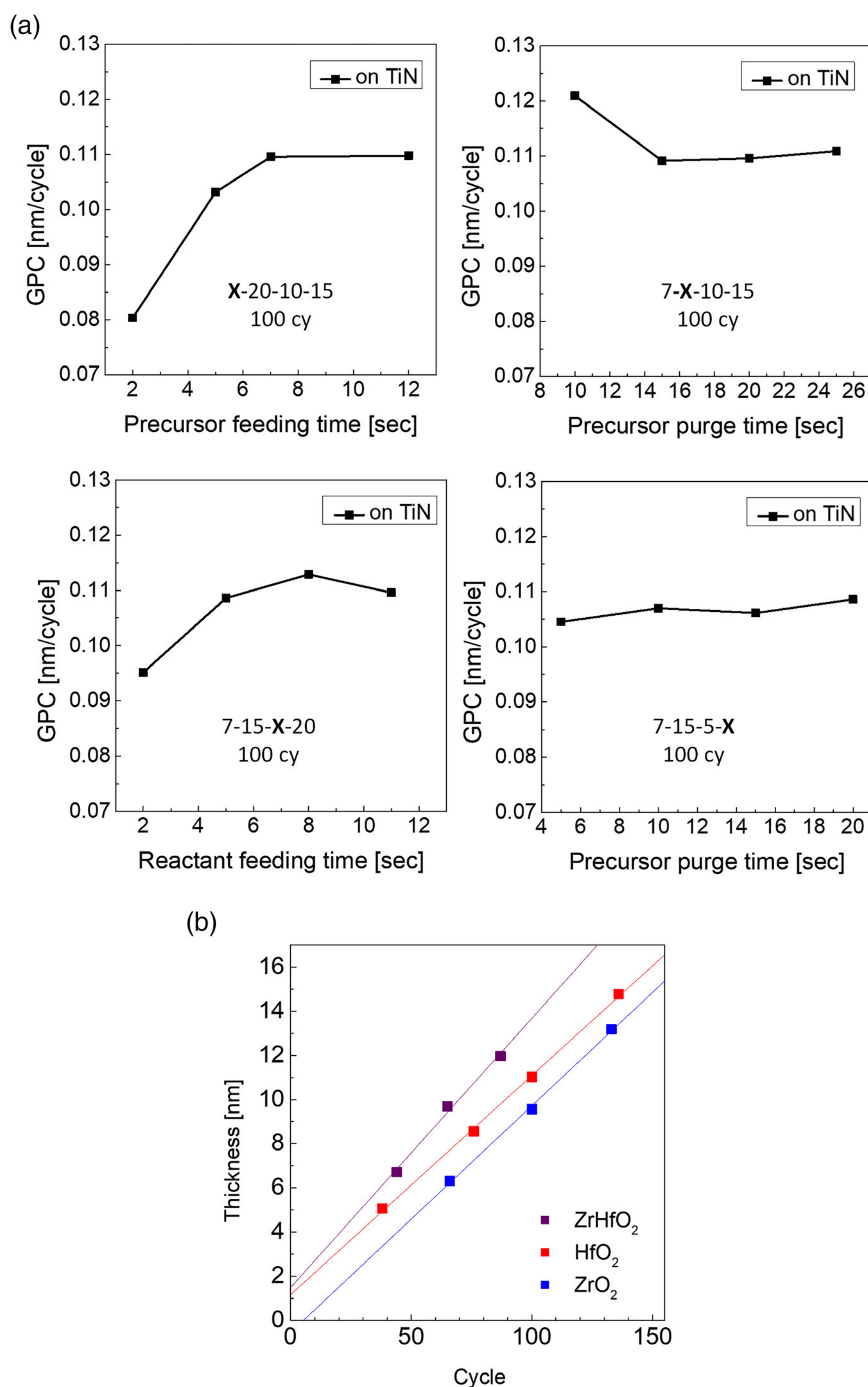

Figure 2. a) Variation of growth per cycle (GPC) with $ZrHfO_2$ atomic layer deposition (ALD) process and b) growth rate of $ZrHfO_2$, HfO_2, and ZrO_2.

has a homogeneous distribution of both Zr and Hf in the entire region. The depth profile analysis shows that the concentration of Zr (as well as Hf) at all composition ratios was constant along the depth direction even after PDA (Figure 3c and S2b, Supporting Information). In contrast, the mixture thin films separately deposited by general ALD supercycles showed large concentration gradients with peaks in the depth profile.[46] The oxygen stoichiometry of the thin films measured at the edge time of 10 s was also confirmed to be constant at 1.8–1.9 after accounting for surface contamination (Figure 3d). Therefore, $ZrHfO_2$ with a homogeneous concentration profile was successfully achieved by introducing a mixed precursor.

To investigate the crystal structure of the homogeneous $ZrHfO_2$ thin films, the XRD spectrum of 6.5-ZHO was compared with those of the ZrO_2-, HfO_2-, and ZrO_2/HfO_2-laminated structure thin films with identical concentrations (Zr concentration = 71 at%) after PDA. The XRD spectra of the thin films are shown in **Figure 4**a. HfO_2 contains several crystal phases where

 © 2022 Wiley-VCH GmbH

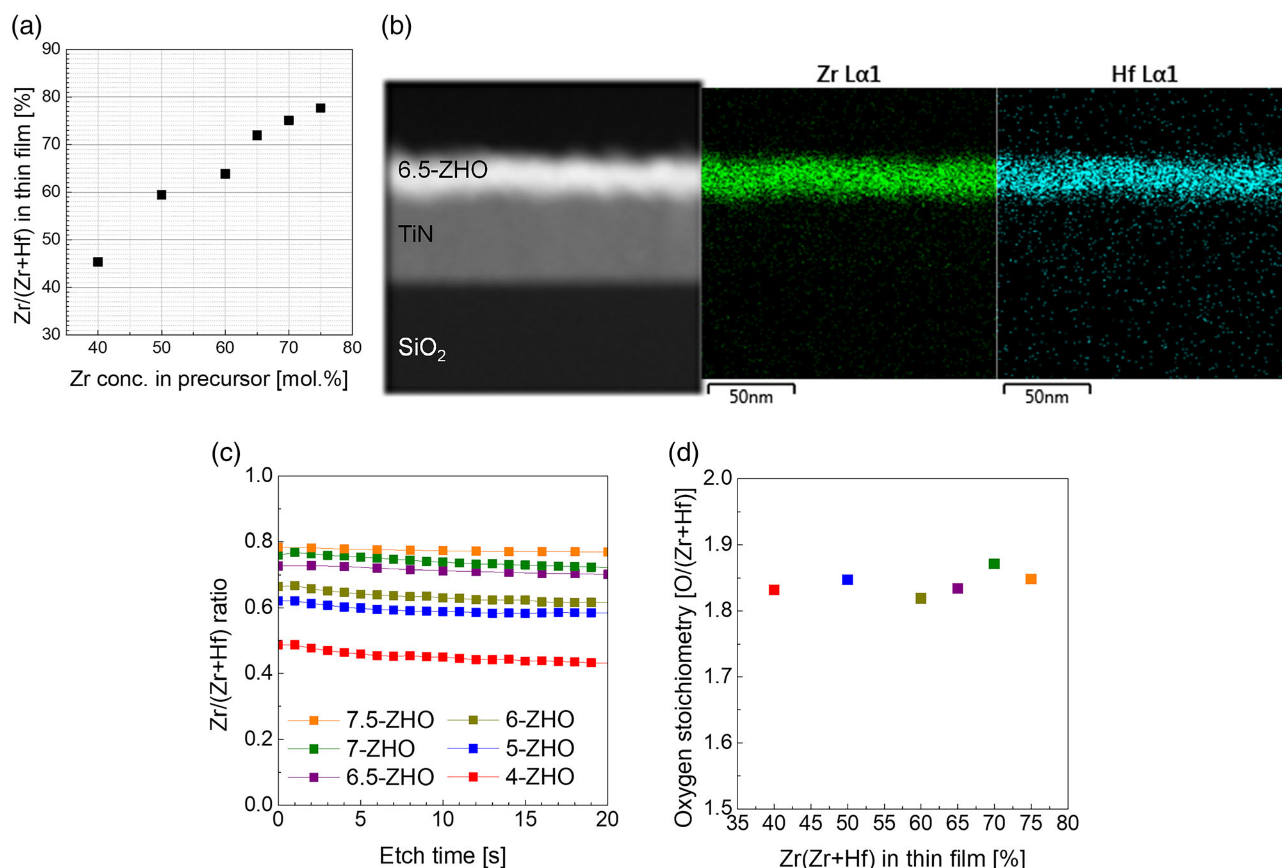

Figure 3. a) Zr/(Zr + Hf) concentration ratio in the deposited thin films, b) transmission electron microscopy energy-dispersive X-ray spectroscopy (TEM-EDX) analysis images for the 6.5-ZHO thin film, c) X-Ray photoelectron spectroscopy (XPS) depth profiles of Zr, and d) oxygen stoichiometry of the thin films.

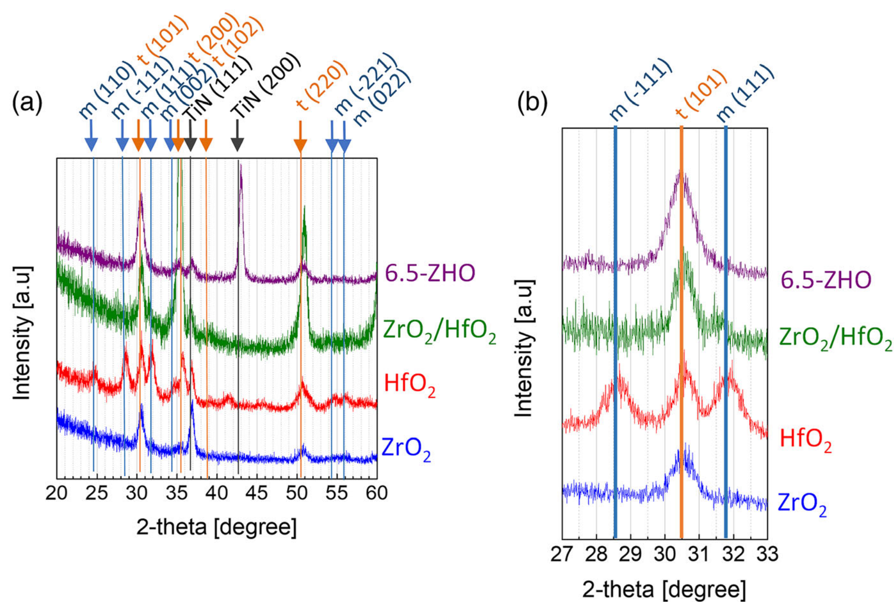

Figure 4. a) X-ray diffraction (XRD) spectra of $ZrHfO_2$ deposited by using a mixed precursor, laminated ZrO_2/HfO_2, HfO_2, and ZrO_2, and b) magnified spectra in vicinity of the major peaks.

© 2022 Wiley-VCH GmbH

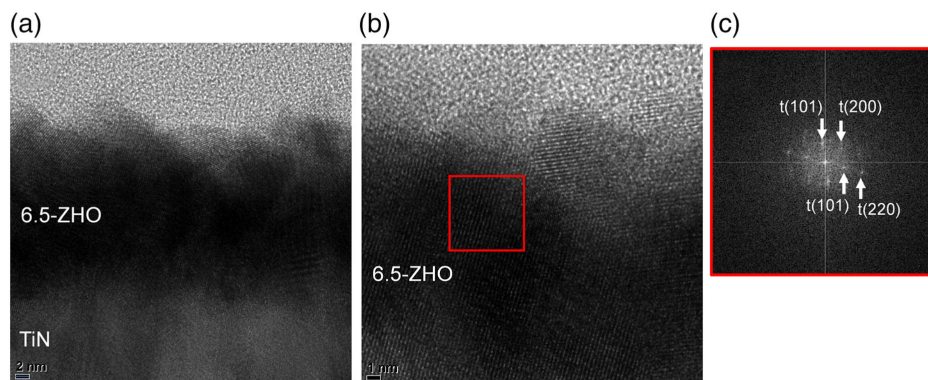

Figure 5. a) Cross-section high-resolution TEM (HR-TEM) image of TiN/6.5-ZHO stack. b) Magnified HR-TEM image of 6.5-ZHO layer. c) Fast-Fourier-transform (FFT) pattern of an indicated region (red box in (b)) of the 6.5-ZHO thin film.

the monoclinic phase is the major peak, whereas ZrO_2 contains only the tetragonal phase, in agreement with previous studies.[35] As previously mentioned, ZrO_2, which is stable in the tetragonal phase in the as-deposited films, stabilizes the tetragonal phase of HfO_2. It was confirmed that the ZrO_2/HfO_2 structure crystallized mostly in the t-phase. However, some monoclinic phases that correspond to t(101) could be observed at 31.7° in the vicinity of the major peaks at 30.5°, although the Zr:Hf composition of this film was approximately 7:3 (Figure 4b). This result indicates that a portion of the HfO_2 that was unaffected by ZrO_2 crystallized in the monoclinic phase because of the inhomogeneous concentration of the thin film deposited in separate parts by general ALD. In contrast, the $ZrHfO_2$ deposited using the mixed precursor exhibited a complete transformation to the tetragonal phase as shown in the XRD pattern of the 6.5-ZHO. No peak corresponding to the m-phase was observed. Moreover, TEM analysis was employed to confirm the crystal structure of the 6.5-ZHO thin film. **Figure 5**a exhibits a stack of 13 nm thick 6.5-ZHO and TiN substrate. As shown in a high-resolution TEM image (Figure 5b), the 6.5-ZHO thin film was highly crystallized. The fast-Fourier-transform (FFT) pattern of the 6.5-ZHO thin film (Figure 5c) consisted of diffraction points corresponding only to the t-phase of (101), (200), and (220) planes. As shown in **Figure 6**a,b, even for 4-ZHO, for which the Zr concentration measured by XPS was 45.4 at%. This means that the well-distributed Hf was transformed effectively from the monoclinic to the tetragonal phase by Zr. This is consistent with the results of first principles calculations in which the random replacement of 50 at% of the Zr atoms with Hf atoms was shown to reduce the relative energies of the tetragonal phase from 5.47 to 4.74 eV and thereby induce the phase stability of the tetragonal phase.[26]

These results are further corroborated by the results of chemical state analysis using XPS measurements. The Hf $4f_{7/2}$ peaks can be deconvoluted into amorphous, monoclinic, and tetragonal peaks because of the different binding energies of the crystal phases.[36] The peak position was recalibrated based on the

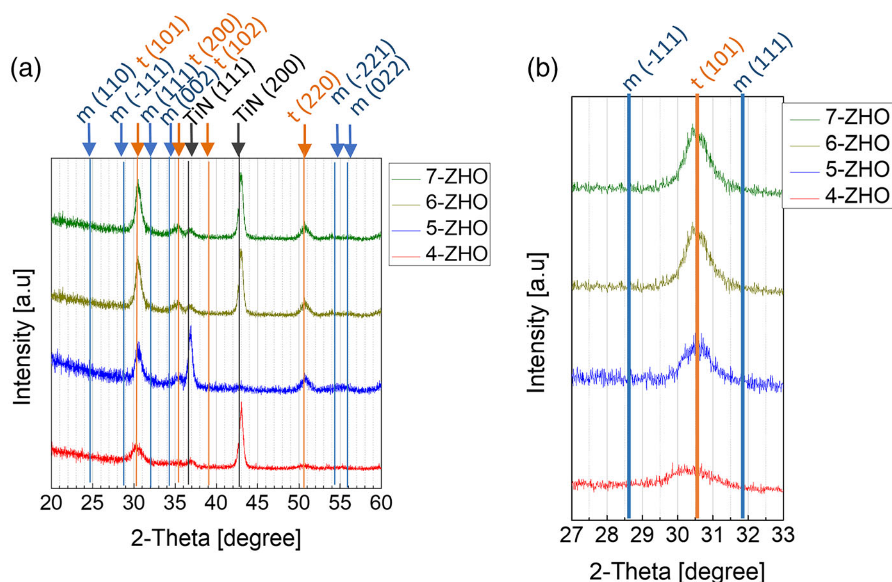

Figure 6. a) XRD spectra of $ZrHfO_2$ at various Zr:Hf compositions, and b) magnified spectra in vicinity of the major peaks.

© 2022 Wiley-VCH GmbH

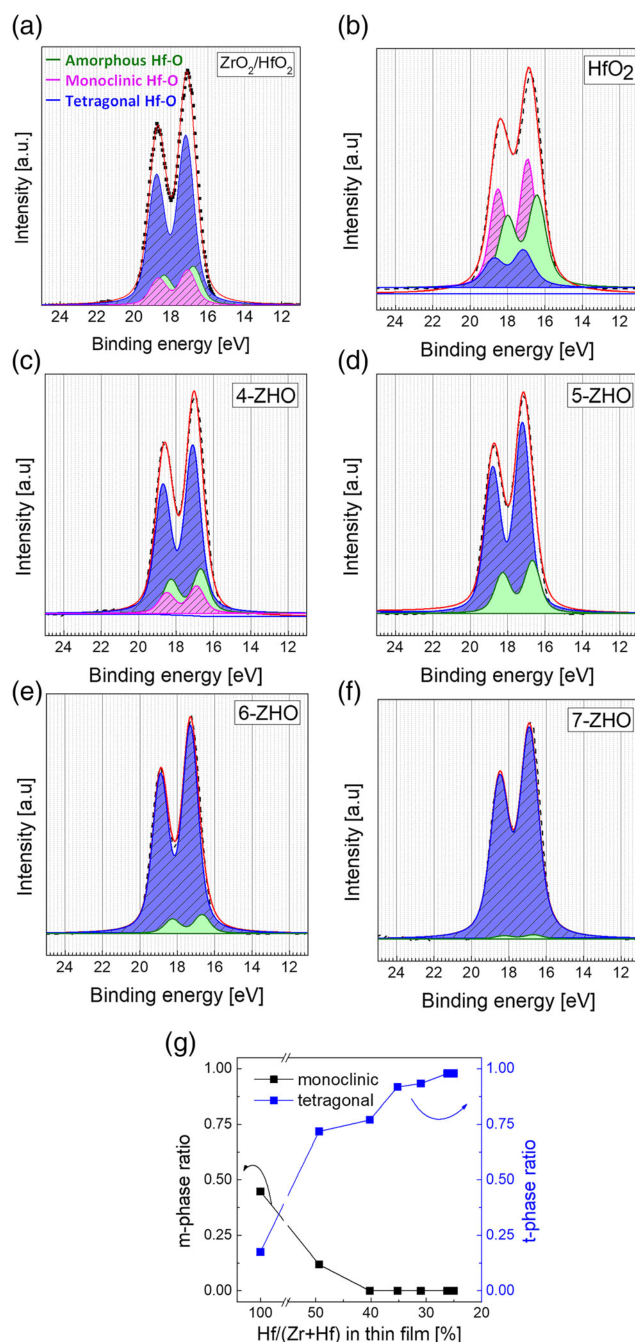

Figure 7. Fitted XPS Hf $4f$ peaks of a) HfO_2, b) ZrO_2/HfO_2, c) 4-ZHO, d) 5-ZHO, e) 6-ZHO, f) 7-ZHO, and g) *m*- and *t*-phase ratio of various ZHO thin films depending on the ratio of Hf.

284.1 eV binding energy of the C—C bond peak position (C 1*s* peak). We assumed that the deconvoluted binding energy peaks of the amorphous, monoclinic, and tetragonal phases were 16.4, 16.9, and 17.1 eV, respectively. **Figure 7** shows the deconvoluted XPS profiles of HfO_2, ZrO_2/HfO_2 with the laminated structure, and homogeneous $ZrHfO_2$ with various compositions. In HfO_2, several peaks corresponding to the tetragonal, monoclinic, and amorphous phases were present. The monoclinic ratio $(m/(m+t+a))$ was 0.45, and the tetragonal ratio $(t/(m+t+a))$ was 0.18, which is consistent with the XRD results (Figure 7a). In ZrO_2/HfO_2, the major peak comprised mainly the tetragonal phase, but the monoclinic phase was also observed with a monoclinic ratio of 0.14, which differs slightly from the very small peaks observed in the XRD measurements. These analysis results show that ZrO_2/HfO_2 was partially grown in the monoclinic phase. In contrast, there were no monoclinic peaks in $ZrHfO_2$ except for 4-ZHO, which had a monoclinic ratio of 0.18. The tetragonal ratios of 4-ZHO, 5-ZHO, 6-ZHO, and 7-ZHO were gradually increased to 0.72, 0.77, 0.92, and 0.98, respectively. In addition, as the Zr concentration increased, the tetragonal peaks increased, and the amorphous peaks decreased. These trends are attributed to the shorter annealing time for crystallization with the increase in the proportion of t-phased ZrO_2 in the as-deposited sample. Therefore, homogeneous $ZrHfO_2$ consisting of only the tetragonal phase can be achieved by using a mixed precursor, even at low Zr contents.

The electrical properties at different degrees of HfO_2 *t*-phase crystallization were evaluated. The *k* value increased from 14.6 in HfO_2, which was mainly in the monoclinic phase, to more than 30 in ZrO_2/HfO_2, ZrO_2, and 6.5-ZHO, which were mainly tetragonal and had the dielectric constants of 34.0, 37.5, and 41.0, respectively (**Figure 8**a). Although ZrO_2/HfO_2 and 6.5-ZHO had the similar Zr concentrations of 71.33 and 71.95 at%, respectively, there is a large difference in their *k* values. It seems that the partially grown *m*-phase in ZrO_2/HfO_2 reduced the dielectric constant, as discussed previously. The leakage current density (J) when 0.8 V of voltage was applied to the capacitor during DRAM operation was evaluated. As shown in Figure 8b, the leakage current densities of ZrO_2/HfO_2, ZrO_2, and 6.5-ZHO at this voltage were 1.80×10^{-7}, 7.46×10^{-8}, 3.23×10^{-8} A cm^{-2}, respectively, which are slightly larger or smaller than the target value of 10^{-7} A cm^{-2} (Figure 8b).

To find the optimal composition, the electrical properties were analyzed for each Zr:Hf composition. The *k* value increased from 35.9 in the 4-ZHO thin film to 36.8, 39.8, and 41.0 when the Zr concentration increased from 5-ZHO to 6-ZHO, and 6.5-ZHO, respectively. The *k* value decreased to 39.9 and 37.3, respectively, which are similar to that of ZrO_2, when the Zr concentration further increased to 7-ZHO and 7.5-ZHO (**Figure 9**a). This implies that the dielectric constant was enhanced by the tetragonal phase transformation of an appropriate amount of HfO_2. To determine the effect of HfO_2 on the dielectric constant of the thin film, the relative dielectric constants were calculated by dividing the total thickness of the thin film into ZrO_2 and HfO_2 components according to the ratio of ZrO_2 and HfO_2 to model the laminated structure and fixing the *k* value of a film consisting of only ZrO_2 to 37.5. Because the capacitors are arranged in a parallel structure in the laminated structure, the partial *k* value can be obtained as $1/C = 1/C_1 + 1/C_2 + \ldots$. The calculated relative dielectric constants of HfO_2 are shown in Figure 9b. The relative *k* values of HfO_2 at the Zr concentrations of 45.4, 59.4, 63.9, 72.0, 75.0, and 77.6 at% in $ZrHfO_2$ were 34.7, 35.8, 44.6, 53.7, 49.4, and 36.8, respectively, whereas that of ZrO_2/HfO_2 was 27.6. As confirmed by the XPS analysis, the *k* values in the thin films decreased with decreasing Zr concentration because of the partial presence of the monoclinic phase and amorphization. The thin films with appropriate HfO_2 contents could thus be

 © 2022 Wiley-VCH GmbH

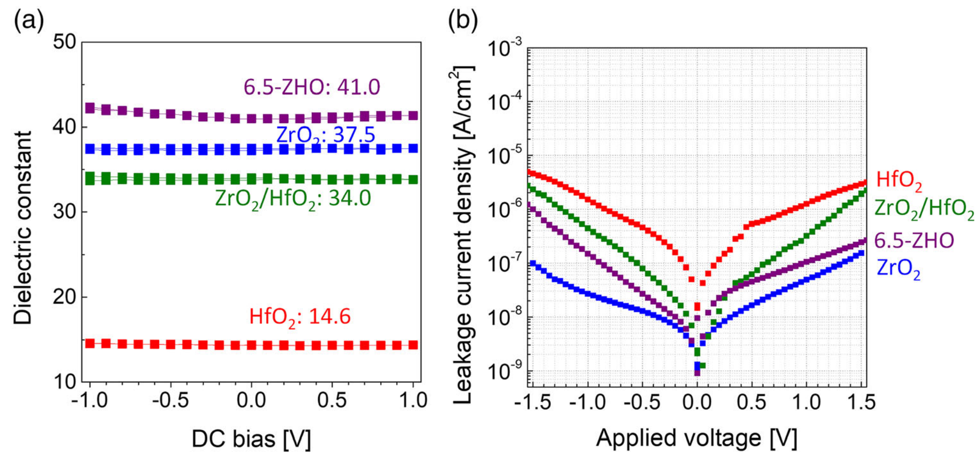

Figure 8. a) Dielectric constants of 6.5-ZHO, ZrO_2, ZrO_2/HfO_2, and HfO_2. b) Leakage current density of each thin film.

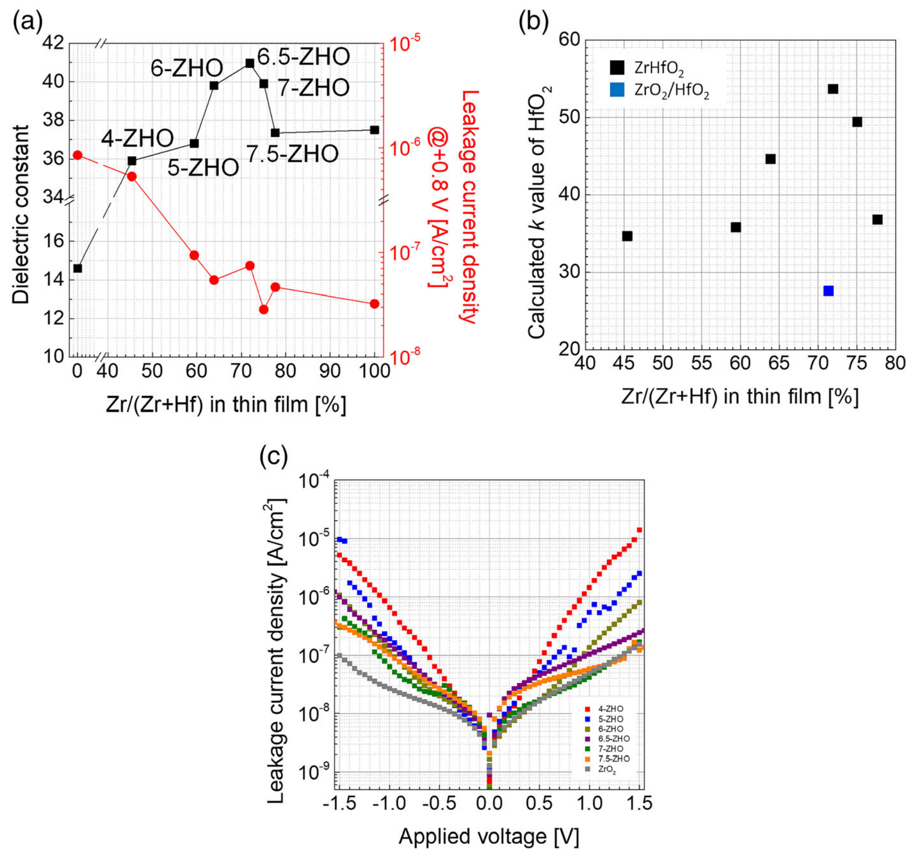

Figure 9. a) Dielectric constant (black, left axis) and leakage current density at applied voltage of +0.8 V (red, right axis) versus Zr/(Zr + Hf), b) relative dielectric constants of HfO_2 in the $ZrHfO_2$ thin films, and c) *J–V* curves of ZrO_2 and $ZrHfO_2$ thin films.

effectively transformed to the tetragonal phase and achieved the *k* value of 41.0 at the Zr concentration of 72.0 at%. Above this Zr concentration, the influence of Zr gradually increased and the *k* values became similar to that of the ZrO_2 single thin film. The leakage current density of the $ZrHfO_2$ thin film also improved as the Zr content increased (Figure 9a,c). Pristine HfO_2 and 4-ZHO exhibited the respective leakage current ensities of 8.52×10^{-7} and 5.32×10^{-7} A cm^{-2}, which exceed 10^{-7} A cm^{-2}, whereas Zr contents above that of 4-ZHO reduced the current densities to 9.39×10^{-8}, 5.43×10^{-8}, 7.47×10^{-8}, 2.85×10^{-8}, and 4.66×10^{-8} A cm^{-2}, which are lower than 10^{-7} A cm^{-2}, in 5-ZHO, 6-ZHO, 6.5-ZHO, 7-ZHO, and 7.5-ZHO, respectively. The results are summarized in **Table 1**. Thus, as the *k* value increased, the equivalent oxide thickness

 © 2022 Wiley-VCH GmbH

Table 1. Summary of thin-film Zr concentration, dielectric constant, and leakage current density at 0.8 V.

	Zr concentration [%]	Dielectric constant	Leakage current density @ + 0.8 V [A cm^{-2}]
HfO_2	0	14.6	5.32×10^{-7}
ZrO_2	100	37.5	3.29×10^{-8}
ZrO_2/HfO_2	71.0	34.0	1.80×10^{-7}
4-ZHO	45.4	35.9	5.32×10^{-7}
5-ZHO	59.4	36.8	9.39×10^{-8}
6-ZHO	63.9	39.8	5.43×10^{-8}
6.5-ZHO	72.0	41.0	7.46×10^{-8}
7-ZHO	75.1	39.9	2.85×10^{-8}

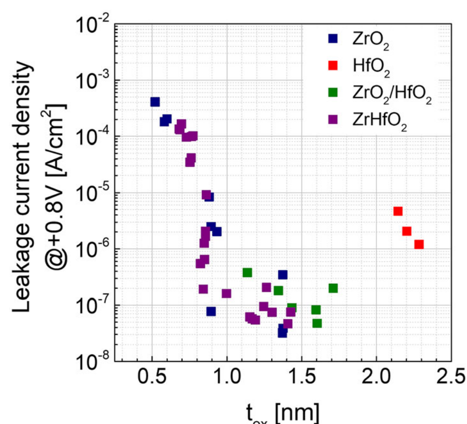

Figure 10. J–t_{ox} plot of the MIM capacitor using 13 nm thick ZrO_2, HfO_2, ZrO_2/HfO_2, and $ZrHfO_2$ thin films.

(t_{ox}) of $ZrHfO_2$ decreased significantly compared to that of the laminated structure to smaller than 1 nm, as shown in the J–t_{ox} plot (**Figure 10**).

3. Conclusion

In this study, $ZrHfO_2$ thin films prepared using a mixed precursor consisting of CpZr and CpHf for DRAM capacitor dielectric applications were investigated. The mixed precursor cannot be used in conventional ALD because of the different evaporation conditions of the precursor components. The ALD deposition of thin films with controlled concentrations, including those with a mixed precursor, using a liquid delivery system, was demonstrated. An additional benefit of this ALD process is the higher GPC achieved compared with general ALD. The deposited $ZrHfO_2$ thin film showed a highly homogeneous concentration profile in the depth direction compared to the ALD supercycle process as well as a crystal structure consisting completely of the tetragonal phase without any monoclinic phase. The deposited film was further investigated through chemical state analysis. The $ZrHfO_2$ thin film with the optimized composition ratio (Zr:Hf = 6.5:3.5) achieved a k value of 41, which is higher than the k values of other thin films. This enhancement was induced by the stabilized tetragonal phase of HfO_2. The highly homogeneous $ZrHfO_2$ thin film resulted in improved capacitor performance in metal–insulator–metal (MIM) capacitors. The adoption of the Zr + Hf mixed precursor is expected to improve capacitor performance not only in DRAM applications but also in other capacitor applications in which Hf and Zr are used.

4. Experimental Section

SiO_2/Si(100) wafer was prepared via chemical vapor deposition. Dielectric $Zr_xHf_{(1-x)}O_2$ thin-film layers were deposited by ALD (iOV dX1, iSAC research) using mixed precursors consisting of cyclopentadienyl tris (dimethylamino) zirconium ($ZrCp[NMe_2]_3$, CpZr) as the Zr precursor and cyclopentadienyl tris (dimethylamino) hafnium ($HfCp[NMe_2]_3$, CpHf) as the Hf precursor at various composition ratios (Zr concentrations of 40, 50, 60, 65, 70, and 75 mol%). To avoid confusion, a specific composition of the $Zr_xHf_{(1-x)}O_2$ thin film is referred to as a-ZHO, where a represents the Zr concentration in the mixed precursor, while $Zr_xHf_{(1-x)}O_2$ thin films in general is collectively referred to as $ZrHfO_2$ in the following. To utilize the mixed precursor during the ALD process, a liquid delivery system (iLD S1, iSAC research) was employed to control the composition of mixed precursors with different evaporation properties through the rapid and simultaneous evaporation of the precursors. The injection of the liquid precursor was controlled by a liquid mass flow controller (LMFC) at 0.05 g min^{-1}. The precursor was vaporized by a vaporizer at 145 °C with an Ar flow of 100 sccm as the carrier gas. The ALD process temperature was 300 °C and the sequence consisted of precursor feeding, Ar purging, ozone feeding at a concentration of 180 g m^{-3}, and Ar purging for 7, 15, 5, and 10 s, respectively. For comparison, 13 nm thick ZrO_2-, HfO_2-, and ZrO_2/HfO_2-laminated thin films were deposited via conventional thermal ALD at 300 °C using $ZrCp(NMe_2)_3$, $HfCp(NMe_2)_3$, and ozone as the Zr precursor, Hf precursor, and oxygen sources, respectively. The laminated structure comprised stacks of 0.5 nm thick HfO_2 and 1 nm thick ZrO_2. PDA was performed at 600 °C for 30 s under N_2-ambient conditions using rapid thermal annealing. For the electrical measurements, which were performed on an MIM capacitor structure, Pt (50 nm)/Ti (50 nm) films were deposited on the top electrode that was defined by a metal shadow mask with a 300 μm diameter hole.

The thicknesses of the insulator films were characterized via a spectroscopic ellipsometer (ESM-300, J. A. Woollam) and X-ray fluorescence (XRF, Thermo Scientific, ARL Quant'X). The depth profiles, composition, and chemical states of the thin films were analyzed using XPS (K-Alpha +, Thermo Fisher Scientific). Glancing angle incident X-ray diffraction (XRD, X'pert Pro, PANalytical) was used to examine the crystal structure of the films at the incident angle of 0.5°. The micro structure of thin film was also examined using TEM (JEM-2100F). The capacitance–voltage (C–V) and leakage current density–voltage (J–V) characteristics were investigated using an Agilent 4284 system and an Agilent 4155C system, respectively.

Supporting Information

Supporting Information is available from the Wiley Online Library or from the author.

Acknowledgements

This work was supported by the Technology Innovation Program (Grant nos. 20003555, 20016813—Development of the ALD precursor with high thermal resistance for improving the dielectric thin-film characteristics for DRAM capacitor, and 20017216) funded by the Ministry of Trade, Industry & Energy (MOTIE, Korea), and Korea Institute of Energy Technology Evaluation and Planning (KETEP) grant funded by the Korea government (MOTIE) (Grant no. 20201520300140, Development

© 2022 Wiley-VCH GmbH

of Advanced Functional Material with C-14 from PHWR Waste). W. J. also acknowledges financial support by a grant from the Kyung Hee University in 2020 (Grant no. KHU-20201107).

Conflict of Interest

The authors declare no conflict of interest.

Data Availability Statement

The data that support the findings of this study are available from the corresponding author upon reasonable request.

Keywords

atomic layer deposition, hafnium oxide, homogeneous thin film, insulator, mixed precursor, zirconium oxide

Received: October 4, 2021
Revised: March 12, 2022
Published online:

[1] R. D. Clark, *Materials* **2014**, *7*, 2913.
[2] C. S. Hwang, *Adv. Electron. Mater.* **2015**, *1*, 1400056.
[3] W. Jeon, *J. Mater. Res.* **2020**, *35*, 775.
[4] S. K. Kim, M. Popovici, *MRS Bull.* **2018**, *43*, 334.
[5] W. Weinreich, A. Shariq, K. Seidel, J. Sundqvist, A. Paskaleva, M. Lemberger, A. J. Bauer, *J. Vac. Sci. Technol. B* **2013**, *31*, 01A109.
[6] Y. W. Yoo, W. Jeon, W. Lee, C. H. An, S. K. Kim, C. S. Hwang, *ACS Appl. Mater. Interfaces* **2014**, *6*, 22474.
[7] S. Y. Lee, J. Chang, Y. Kim, H. J. Lim, H. Jeon, H. Seo, *Appl. Phys. Lett.* **2014**, *105*, 2.
[8] M. Pešić, S. Knebel, M. Geyer, S. Schmelzer, U. Böttger, N. Kolomiiets, V. V. Afanas'ev, K. Cho, C. Jung, J. Chang, H. Lim, T. Mikolajick, U. Schroeder, *J. Appl. Phys.* **2016**, *119*, 064101.
[9] H. J. Cho, Y. D. Kim, D. S. Park, E. Lee, C. H. Park, J. S. Jang, K. B. Lee, H. W. Kim, Y. J. Ki, I. K. Han, Y. W. Song, *Solid State Electron.* **2007**, *51*, 1529.
[10] C. H. An, W. Lee, S. H. Kim, C. J. Cho, D.-G. Kim, D. S. Kwon, S. T. Cho, S. H. Cha, J. I. Lim, W. Jeon, C. S. Hwang, *Phys. Status Solidi RRL* **2019**, *13*, 1800454.
[11] S. K. Kim, S. W. Lee, J. H. Han, B. Lee, S. Han, C. S. Hwang, *Adv. Funct. Mater.* **2010**, *20*, 2989.
[12] S. K. Kim, G. J. Choi, S. Y. Lee, M. Seo, S. W. Lee, J. H. Han, H. S. Ahn, S. Han, C. S. Hwang, *Adv. Mater.* **2008**, *20*, 1429.
[13] W. Jeon, S. Yoo, H. K. Kim, W. Lee, C. H. An, M. J. Chung, C. J. Cho, S. K. Kim, C. S. Hwang, *ACS Appl. Mater. Interfaces* **2014**, *6*, 21632.
[14] W. Jeon, S. H. Rha, W. Lee, Y. W. Yoo, C. H. An, K. H. Jung, S. K. Kim, C. S. Hwang, *ACS Appl. Mater. Interfaces* **2014**, *6*, 7910.
[15] S. W. Lee, J. H. Han, S. Han, W. Lee, J. H. Jang, M. Seo, S. K. Kim, C. Dussarrat, J. Gatineau, Y.-S. Min, C. S. Hwang, *Chem. Mater.* **2011**, *23*, 2227.
[16] D. K. Joo, J. S. Park, S. W. Kang, *Electrochem. Solid-State Lett.* **2009**, *12*, 77.
[17] T. Nabatame, A. Ohi, T. Chikyo, M. Kimura, H. Yamada, T. Ohishi, *J. Vac. Sci. Technol. B* **2014**, *32*, 03D121.
[18] D.-K. Lee, S.-H. Kwon, J.-H. Ahn, *Mater. Lett.* **2019**, *246*, 1.
[19] S. H. Cha, C. H. An, S. T. Cho, D.-G. Kim, D. S. Kwon, J. Il Lim, W. Jeon, C. S. Hwang, *Phys. status solidi RRL* **2019**, *13*, 1900282.
[20] T. T. Le, J. G. Ekerdt, *J. Vac. Sci. Technol. A* **2020**, *38*, 032401.
[21] W. Jeon, W. Lee, Y. W. Yoo, C. H. An, J. H. Han, S. K. Kim, C. S. Hwang, *J. Mater. Chem. C* **2014**, *2*, 9993.
[22] S. K. Kim, W. D. Kim, K. M. Kim, C. S. Hwang, J. Jeong, *Appl. Phys. Lett.* **2004**, *85*, 4112.
[23] B. Kim, Y. Choi, D. Lee, S. Cheon, Y. Byun, H. Jeon, *Nanotechnology* **2022**, *33*, 115701.
[24] T. H. Perng, C. H. Chien, C. W. Chen, P. Lehnen, C. Y. Chang, *Thin Solid Films* **2004**, *469–470*, 345.
[25] H. Hu, C. Zhu, Y. F. Lu, M. F. Li, B. J. Cho, W. K. Choi, *IEEE Electron Device Lett.* **2002**, *23*, 514.
[26] S. W. Jeong, H. J. Lee, K. S. Kim, M. T. You, Y. Roh, T. Noguchi, W. Xianyu, J. Jung, *Thin Solid Films* **2006**, *515*, 526.
[27] D. Y. Cho, H. S. Jung, I. H. Yu, J. H. Yoon, H. K. Kim, S. Y. Lee, S. H. Jeon, S. Han, J. H. Kim, T. J. Park, B. G. Park, C. S. Hwang, *Chem. Mater.* **2012**, *24*, 3534.
[28] T. S. Böscke, S. Govindarajan, C. Fachmann, J. Heitmann, A. Avellán, U. Schröder, S. Kudelka, P. D. Kirsch, C. Krug, P. Y. Hung, S. C. Song, B. S. Ju, J. Price, G. Pant, B. E. Gnade, W. Krautschneider, B. H. Lee, R. Jammy, *Technical Digest-International Electron Devices Meeting, IEDM*, San Francisco, CA, USA, 13 December **2006**, p. 8.
[29] K. Tomida, K. Kita, A. Toriumi, *Appl. Phys. Lett.* **2006**, *89*, 142902.
[30] P. K. Park, S.-W. Kang, *Appl. Phys. Lett.* **2006**, *89*, 192905.
[31] A. Payne, O. Brewer, A. Leff, N. A. Strnad, J. L. Jones, B. Hanrahan, *Appl. Phys. Lett.* **2020**, *117*, 221104.
[32] N. Haratipour, Y. Liu, R. J. Wu, S. Namgung, P. P. Ruden, K. A. Mkhoyan, S.-H. Oh, S. J. Koester, *IEEE Trans. Electron Devices* **2018**, *65*, 4093.
[33] C. Fan, F.-P. Tseng, C. Tseng, *Materials* **2018**, *11*, 824.
[34] M. N. K. Alam, S. Clima, B. J. O'sullivan, B. Kaczer, G. Pourtois, M. Heyns, J. Van Houdt, *J. Appl. Phys.* **2021**, *129*, 084102.
[35] M. M. Rahman, J. G. Kim, D. H. Kim, T. W. Kim, *Micromachines* **2019**, *10*, 1.
[36] C.-K. Lee, E. Cho, H.-S. Lee, C. S. Hwang, S. Han, *Phys. Rev. B* **2008**, *78*, 012102.
[37] J. H. Ahn, S. H. Kwon, *ACS Appl. Mater. Interfaces* **2015**, *7*, 15587.
[38] T. S. Böscke, P. Y. Hung, P. D. Kirsch, M. A. Quevedo-Lopez, R. Ramírez-Bon, *Appl. Phys. Lett.* **2009**, *95*, 2007.
[39] M. Materano, C. Richter, T. Mikolajick, U. Schroeder, *J. Vac. Sci. Technol. A* **2020**, *38*, 022402.
[40] H. S. Jung, S. A. Lee, S. H. Rha, S. Y. Lee, H. K. Kim, D. H. Kim, K. H. Oh, J. M. Park, W. H. Kim, M. W. Song, N. I. Lee, C. S. Hwang, *IEEE Trans. Electron Devices* **2011**, *58*, 2094.
[41] M. H. Park, Y. H. Lee, H. J. Kim, Y. J. Kim, T. Moon, K. Do Kim, S. D. Hyun, C. S. Hwang, *ACS Appl. Mater. Interfaces* **2018**, *10*, 42666.
[42] H. C. M. Knoops, T. Faraz, K. Arts, W. M. M. (Erwin) Kessels, *J. Vac. Sci. Technol. A* **2019**, *37*, 030902.
[43] P. D. Lomenzo, Q. Takmeel, C. Zhou, C. C. Chung, S. Moghaddam, J. L. Jones, T. Nishida, *Appl. Phys. Lett.* **2015**, *107*, 242903.
[44] D. Chan Won, S.-W. Rhee, *J. Vac. Sci. Technol. B* **2014**, *32*, 03D102.
[45] J. Niinistö, M. Mäntymäki, K. Kukli, L. Costelle, E. Puukilainen, M. Ritala, M. Leskelä, *J. Cryst. Growth* **2010**, *312*, 245.
[46] J. Ho Lee, I.-H. Yu, S. Young Lee, C. Seong Hwang, *J. Vac. Sci. Technol. B* **2014**, *32*, 03D109.

© 2022 Wiley-VCH GmbH